sustainability

MDPI

Article

Characterization of South African Bentonite and Kaolin Clays

Dipuo P. Kgabi and Abayneh A. Ambushe *

Department of Chemical Sciences, University of Johannesburg, P.O. Box 524, Auckland Park, Johannesburg 2006, South Africa; dipuopreciouskgabi@gmail.com
* Correspondence: aambushe@uj.ac.za

Abstract: The present study aimed to investigate the mineralogical and morphological properties of two South African clays, namely bentonite and kaolin. These clays are mined in specific regions of the country but have not been fully characterized in terms of their properties for potential application in a number of industries. Bentonite was found to have a larger specific surface area, pore size, and more interchangeable cations than kaolin. The bentonite was also identified as Na-bentonite due to the huge Na content present in the clay. The powder X-ray diffraction (PXRD) patterns revealed that both clays are crystalline, together with the Fourier-transform infrared (FTIR) spectrophotometer results; presumably, some impurities of quartz could be present in the clay materials. The most prevalent functional groups present include Al-OH, Si-O-Mg, Si-O, and Si-O-Al groups. The surface charge of bentonite was consistently negative across all pH values, indicating its potential for adsorption applications. On the other hand, kaolin exhibited a negative charge at pH values greater than 2.4. The scanning electron microscopy (SEM) images provided visual evidence of the presence of pores in the clay structures, which supported the Brunauer–Emmett–Teller (BET) results classifying both bentonite and kaolin as mesoporous and macroporous materials. The particle size analysis revealed a broad distribution for bentonite and a bimodal distribution for kaolin. Overall, the clays revealed interesting features that can be useful for application in several industries, for example, in the treatment of wastewater. Further research and development can explore their potential to address environmental challenges, particularly the application of bentonite and kaolin in water treatment processes to remove toxic metal ions.

Keywords: bentonite; characterization; clay; kaolin; South Africa

check for updates

Citation: Kgabi, D.P.; Ambushe, A.A. Characterization of South African Bentonite and Kaolin Clays. *Sustainability* **2023**, *15*, 12679. https://doi.org/10.3390/su151712679

Academic Editor: Marco Lezzerini

Received: 20 June 2023
Revised: 16 August 2023
Accepted: 16 August 2023
Published: 22 August 2023

1. Introduction

Clay is a naturally occurring phyllosilicate material with varying water content and containing different cations, such as sodium, alkali metals, and iron [1]. The presence of these cations can result in a wide range of chemical compositions for clay minerals through substitutions of aluminum for magnesium and iron [2]. Clays are classified into different groups based on their structural arrangements and chemical compositions, and these properties determine their applications [2,3]. Two examples of clay groups are smectite and kaolinite.

Smectites, including minerals like montmorillonite, saponite, hectorite, nantronite, and beidellite, belong to the hydroxy alumino-silicate group and are formed through the weathering of soil, rock, or volcanic ash [3,4]. Chemical substitution, exchangeable cations, and impurities can influence the physical and chemical properties of smectites [5]. Smectites are often associated with minerals such as quartz, kaolinite, feldspars, volcanic glass, and zeolites [1]. Their composition can vary, with Mn^{2+}, Mg^{2+}, or Fe^{2+} substituting Al^{3+} in the octahedral cation sites and Fe^{3+} or Al^{3+} replacing Si^{4+} in the tetrahedral cation sites [1,5]. Smectites possess thin layers and small particle sizes, which contribute to their high adsorptive properties for water, oil, and chemicals [6,7]. They exhibit characteristics like swelling, shrinkage, and high cation exchange capacity (CEC) [8,9]. The presence of

interlayer cations affects their swelling behavior, with sodium-containing clays demonstrating higher expansion capacity [10]. Smectites possess valuable properties such as catalytic activity, high CEC, specific surface area, adsorptive capacity, and surface reactivity, making them useful in various industries [4,11].

Kaolinite, on the other hand, is a 1:1 clay mineral formed under acidic conditions through the weathering of aluminosilicates. It has strong interlayer forces that make it resistant to expansion when wet [12,13]. Compared to montmorillonite, kaolinite has a lower CEC due to its low specific surface area and minimal isomorphous substitution, resulting in high molecular stability, low shrinkage, plasticity, swelling, and cohesion [1,13].

Both smectite and kaolinite clays find numerous applications across various industries. Kaolin's exceptional electrical insulating properties, along with the mentioned attributes, render it well-suited for manufacturing porcelain insulators used in electrical applications. Additionally, kaolin finds application in the creation of white cement, serving as a source of iron-free alumina, and in the production of glass fiber as a low-iron, low-alkali alumina resource [1]. Bentonite finds application in various areas, including binding foundry sands, formulating drilling fluids, pelletizing iron ore, creating adhesives, and facilitating decolorization [13]. Additionally, it serves as a clarifying agent for oils and fats and holds utility as both a chemical barrier and a liquid barrier [14]. Both clays are used in agriculture as carriers for fertilizers, pesticides, and seed coatings. Other applications include papermaking, paints, cosmetics, ceramics, and catalytic, and they also serve as adsorbents for organic and inorganic contaminants [2,7,12,13,15–18]. These clays may contain impurities in their structure, such as illite, quartz, anatase, graphite, rutile, zircon, halloysite, mica, siliminate, titaniferous, carbonaceous material, and feldspar [1,12]. These impurities can affect the suitability of the clay for certain applications. Therefore, when evaluating clay samples, it is essential to combine mineralogical examination with visual assessment, followed by beneficiation trials and product evaluation. This process helps to identify and sort out samples with inferior properties.

Several studies have been performed on characterizing some South African clays for different applications. Studies by Mulaba-Bafubiandi and Hlekane [19] and Diko-Makia and Ligege [20] characterized South African clays for their bulk density, shrinkage, water absorption, plasticity, and flexural strength for application in ceramics and pottery. Another study by Coetze et al. [21] looked into the characterization of kaolin, bauxite, palygorskite, laterite, and bentonite for the removal of fluoride (F^-) from water. The study found that many of these South African clays were not efficient adsorbents for F^- (adsorption capacity of 0.40–0.10 mg/g), and kaolin was the poorest adsorbent amongst them (with an adsorption capacity of 0.03 mg/g). Other studies have characterized clay materials for cosmetic purposes, and it was found that the clays had high levels of quartz, which could pose a health hazard when applied to the skin [22]. Although several studies were conducted to characterize clay materials for various applications, little to no studies focused on the characterization of South African clays for the removal of potentially toxic elements (PTEs) from water and wastewater.

This study aimed to characterize, classify, and compare two South African clays, namely bentonite and kaolin, from different deposits using various characterization techniques. The goal is to explore their potential for the removal of PTEs from water and wastewater. Bentonite and kaolin were specifically chosen for this study due to their ease of availability, abundance, and frequent use in other industries. Understanding the physicochemical properties of these clays can expand their applications in various industries. To achieve this, a range of analytical techniques, including thermal gravimetric analysis (TGA), X-ray fluorescence (XRF), energy-dispersive X-ray spectroscopy (EDS), powder X-ray diffraction (PXRD), Fourier-transform infrared (FTIR) spectroscopy, Brunauer–Emmett–Teller (BET) analysis, scanning electron microscopy (SEM), high-resolution transmission electron microscopy (HRTEM), and zetasizer analysis, were employed to investigate the thermal stability, chemical composition, functional groups, mineralogical phases, specific surface area, morphology, zeta potential, and particle size of the clays.

2. Methods and Materials

2.1. Clay Material

The clays used in this study were the 2:1 bentonite clay (CEC = 78 cmol (+)/kg), purchased from Imerys (Pretoria, South Africa) and mined at the Cape Bentonite Mine in Heidelberg town located in the Western Cape province of South Africa. Additionally, the 1:1 kaolin clay (CEC = 13 cmol (+)/kg) was purchased from Micronized (Johannesburg, South Africa) and mined at the Grahamstown Kaolinite complex in the Eastern Cape province of South Africa.

2.2. Instrumentation and Equipment

The morphology of the clays was analyzed using the following instruments: JEOL-JEM 2100 HRTEM (Jeol, Tokyo, Japan), TESCAN VEGA 3 LMH SEM (TESCAN, Brno-Kohoutovice, Czech Republic), and EDS (Oxford Instruments, Buckinghamshire, UK). The crystallinity of the clays was assessed using a PANanalytical Philips X'Pert PXRD (PANanalytical, Almelo, The Netherlands). To identify the functional groups present in the clay materials, an IR Affinity-1S FTIR spectrophotometer (Shimadzu, Kyoto, Japan) was employed. The thermal stability of the clays was determined using an STA 6000 TGA (TA Instruments, New Castle, DE, USA). The specific surface area, pore diameter, and volume of the samples were measured using the Mircromeritics ASAP 2020 Gas Absorption BET (Micrometrics, Brussels, Belgium). The zeta potential and particle size of the clays were determined using the Malvern Zetasizer (Malvern Panalytical, Randburg, South Africa). Borate fusion discs were prepared using the CLAISSE-TheOx Advanced fusion instrument (DKSH group, Zurich, Switzerland). Following fusion, the samples were analyzed using the PANalytical MagiX PRO XRF instrument (Malvern PANalytical, Nottingham, UK).

2.3. Sample Preparation and Analysis Procedures

2.3.1. Scanning Electron Microscopy

For SEM analysis, a small quantity of clay material was placed on carbon tape and coated using an Agar Turbo Carbon Coater. The coated samples were then examined using SEM, equipped with the TESCAN Vega3 TC control software, with a working distance of 15 mm. The shape and surface morphology of the samples were observed by adjusting the magnification and focus settings of the microscope. To determine the elemental composition of the clays, SEM was coupled with EDS, allowing for the identification and quantification of the elements present in the samples.

2.3.2. High-Resolution Transmission Electron Microscopy

High-resolution transmission electron microscopy was employed to acquire detailed insights into the internal structure of the clays. Prior to HRTEM analysis, a small portion of the clay sample was soaked in ethanol and then subjected to agitation in a sonicator for an hour. Subsequently, a small portion of the resulting suspension was placed onto carbon-coated copper grids, which were then examined using HRTEM at a voltage of 200 kV. This allowed for high-resolution imaging and analysis of the clay's internal structure at the atomic level. The particle size distribution from HRTEM images was obtained by analyzing images at different scales using the ImageJ software (version 1.53t).

2.3.3. Powder X-ray Powder Diffraction

The PXRD technique was used to determine the mineralogy and crystal structures of the clays. To conduct PXRD analysis, dried and sieved clay samples were mounted and carefully aligned onto the steel sample holders and placed into the PXRD instrument.

X-rays were diffracted at various angles (2θ) ranging from 0 to 90°. The Cu-Kα radiation source with an energy of 8.04 keV and a wavelength of 0.15406 nm was employed for the analysis. The PXRD analysis was performed at a current of 40 mA and a voltage of 40 kV. The data were processed using the X'Pert HighScore Plus software (version

4.5, PANalytical, Malvern, UK) to generate diffraction patterns, which were then used to identify the constituents and components present in the clay samples.

2.3.4. Fourier-Transform Infrared Spectroscopy

To analyze the clay sample's IR spectra, a small portion of the clay sample was placed in a sample holder and compressed. The sample was then analyzed in the wavenumber range of 400 to 4000 cm^{-1}. Spectra were obtained by scanning the sample 32 times with a resolution of 16 cm^{-1}. The analysis was conducted using an attenuated total reflectance (ATR) probe, eliminating the need for additional sample preparation. This allowed for the collection of IR spectra, providing information about the functional groups present in the clay sample.

2.3.5. Thermal Gravimetric Analysis

An aliquot sample of the clay was introduced into the TGA sample holder. The thermal stability of the clay material was assessed by subjecting it to a temperature range of 25 to 1000 °C under a N_2 atmosphere. As the temperature was gradually increased, the weight loss of the material was measured and recorded. This allowed for the characterization of the thermal behavior of the clay sample and the determination of any weight changes or decomposition processes occurring within the specified temperature range.

2.3.6. Brunauer–Emmett–Teller

Prior to analysis, approximately 0.4 g of the clays were placed in a BET tube. The sample was then subjected to degassing at 90 °C using a N_2 micrometric degassing system for a duration of 12 h. The specific surface area, volume, and pore size of the clay samples were calculated using the BET method at a temperature of −195.8 °C.

2.3.7. Zeta Potential and Particle Size

For zeta potential measurement, approximately 0.02 g of the clay samples were added to 50 mL centrifuge tubes containing water solutions with varying pH values, ranging from 1 to 12. The centrifuge tubes were then sonicated at room temperature for one hour to ensure proper dispersion of the clay particles in the solution. Subsequently, the suspension was transferred to a zetasizer dip cell for zeta potential measurement. The zeta potential of the clay samples was recorded at each pH level, and the relationship between the zeta potential and pH was analyzed and reported.

To determine the particle size of the clays, approximately 0.03 g of the clay samples were dispersed in water following a similar sonication and suspension procedure as described above. The measurements were conducted using the same zetasizer instrument. The zetasizer was set to record measurements at a count rate of 300 kcps for a duration of 60 s at a measurement position of 1.08 mm. This allowed for the determination of the particle size distribution of the clay samples through dynamic light scattering (DLS).

2.3.8. X-ray Fluorescence

About 1.02 g of the clay samples were weighed into glazed porcelain crucibles and heated at 930 °C for 30 min in a muffle furnace. After the ignition process, the samples were cooled in a desiccator containing anhydrous silica gel. The loss on ignition (LOI) was calculated by subtracting the mass of the sample after ignition from the initial mass of the clay sample.

For elemental composition analysis, approximately 0.7 g of the ignited clay samples were mixed with 0.1 g of lithium nitrate ($LiNO_3$) and 6.0 g of 50/50 flux (Malvern PANalytical, Randburg, South Africa) in Pt–Au crucibles. The flux composition consisted of 49.75% mass lithium tetraborate ($Li_2B_4O_7$), 49.75% mass lithium metaborate ($LiBO_2$), and 0.5% mass lithium bromide (LiBr). The mixture of the clay sample, lithium nitrate, and flux was then subjected to fusion in the Claisse TheOx Advanced fusion instrument at a temperature of 1100 °C for 5 min. After fusion, the mixture was allowed to cool, and the

resulting fused sample was cast into a glass bead within the crucible. Following fusion, the samples were analyzed using the PAnalytical MagiX PRO XRF instrument.

3. Results and Discussion

3.1. SEM and TEM Characterization

The morphological properties of the clay structures were investigated using SEM and HRTEM imaging, and the micrographs are shown in Figure 1. The SEM image of bentonite (a) displays porous, spongy-like structures, with some illuminated platelets indicating the presence of quartz [1]. The HRTEM images of bentonite (b) show irregularly shaped structures resembling spheres that are stacked with the presence of latticed fringes highlighted in red. The well-resolved lattice fringes seen in (c) confirm the crystallinity of the clay, as later validated by the PXRD pattern in Figure 2. Similar findings were reported by Abukhadra et al. [23], where the HRTEM image of bentonite revealed multi-layered particles with lattice fringes.

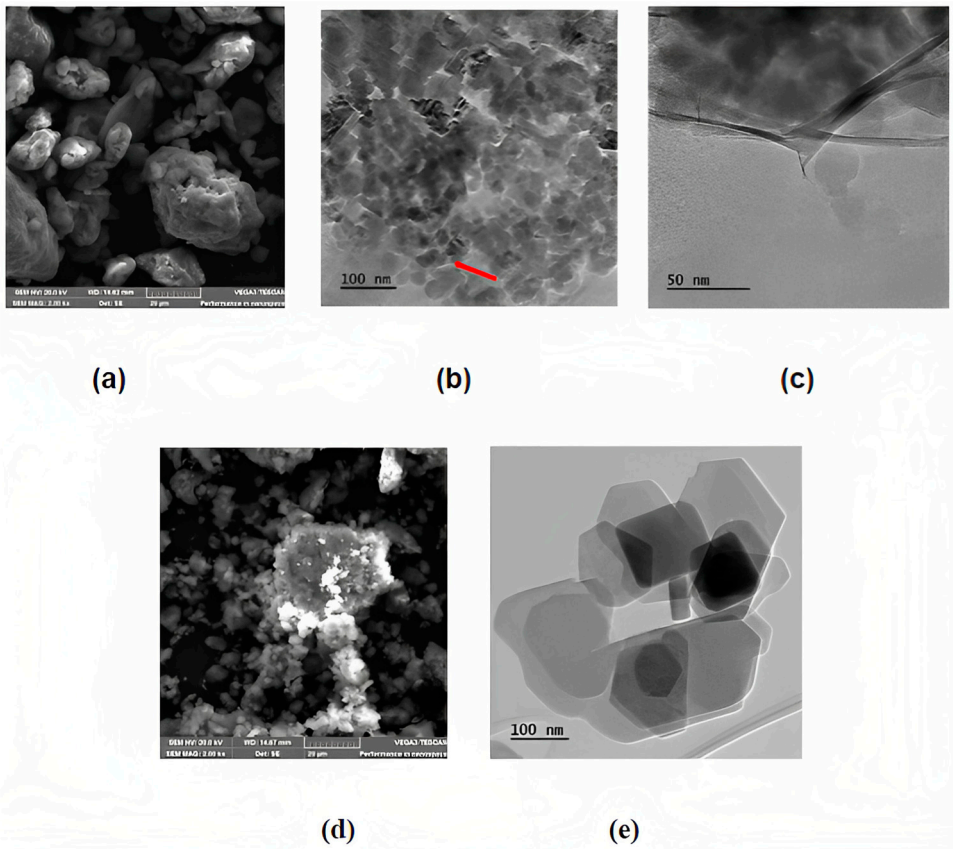

Figure 1. (**a**) SEM image of bentonite; (**b**) HR-TEM image of bentonite; (**c**) SEM image of bentonite with lattice fringes; (**d**) SEM image of kaolin; and (**e**) HR-TEM image of kaolin.

The SEM image of kaolin in Figure 1d displays flaky structures with an irregular shape and a porous texture. Additionally, particle agglomeration is observed. The SEM image of kaolin also reveals the presence of illuminated crystals, which can also be attributed to quartz [24]. The shape of the quartz can be confirmed by the hexagonal structures seen in the image in Figure 1e [25]. The HRTEM and SEM images of both clays show structures of different shapes and sizes, indicating the heterogeneity of the samples.

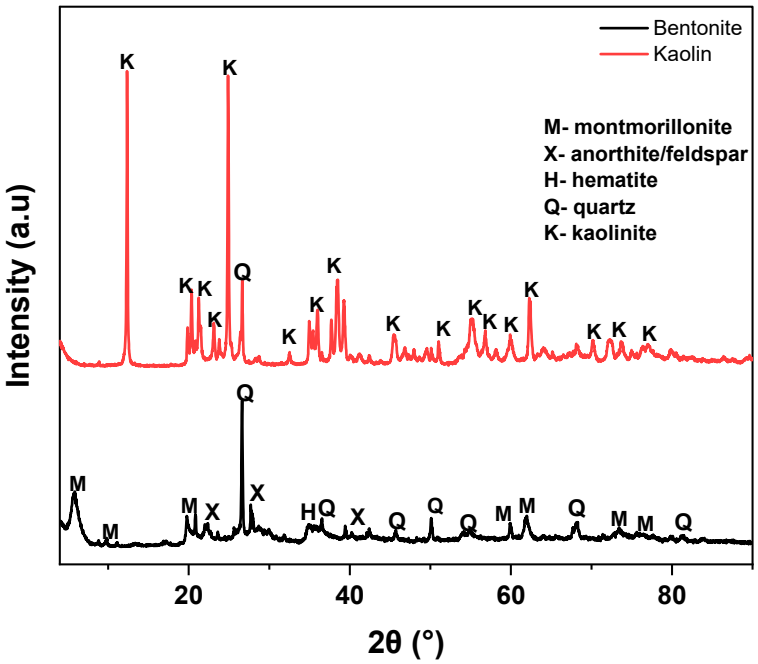

Figure 2. PXRD patterns of bentonite and kaolin.

3.2. PXRD Characterization

The PXRD patterns of bentonite and kaolin clays are depicted in Figure 2. The diffraction peaks observed in the bentonite pattern are indicative of the presence of montmorillonite (M), which appears to be the primary component of the sample. Impurities such as anorthite (A), hematite (H), and quartz (Q) have also been identified in the spectra, consistent with previous reports on similar materials [24,26,27].

The clay minerals were identified by closely analyzing peak intensities and positions and comparing them to the patterns found in the International Tables for Crystallography database. The mineralogical composition of bentonite can be determined by its characteristic reflections. The characteristic peak for montmorillonite (M) was confirmed at a d_{001} value of 17.6 Å. The basal value, d_{001} = 17.6 Å, distinguishes montmorillonite from vermiculite, which occurs at 1.0–1.5 Å [28]. Furthermore, other characteristic peaks of montmorillonite can be observed at d (Å) = 4.49 and 1.50. Similar results were reported elsewhere [16,29]. Quartz reflections are observed at d (Å) = 4.26 and 3.34, while anorthite/feldspar (X) peaks can be observed at d (Å) = 3.19, 4.04, and 3.12. These reflection peaks are similar to those reported by Chandra et al. [30]. Maged et al. [27] and Tadesse [16] also reported similar reflections for anorthite at d (Å) = 3.21 and 4.03.

The PXRD pattern of kaolin reveals sharp and strong peaks corresponding to the kaolinite (K) mineral, along with low-intensity peaks of minor quartz (Q) impurities. The kaolinite peaks exhibit intensity and structural order. The main characteristic reflections of kaolinite are observed at d (Å) = 7.17 and 3.58. The reflections of quartz appear at d = 26.6 Å. These findings are consistent with previous reports by Caponi et al. [31].

3.3. FTIR Spectroscopy Characterization

The functional groups present in the clays were determined using FTIR spectroscopy, and the results are shown in Figure 3.

The FTIR spectrum of bentonite shows a maximum absorption peak at 995 cm^{-1}, which is a characteristic of layered silicate montmorillonite minerals and is assigned to the triply degenerate Si-O stretching vibration [32]. The presence of Al-OH-Mg bonds is observed at 3842 cm^{-1} and 864 cm^{-1}, along with a weak band at 794 $cm^{-1,}$ indicating Fe^{3+}–OH–Mg bonds and suggesting a higher Mg content compared to Fe^{3+} [33]. The band at 690 cm^{-1} can be attributed to the Si-O-Al and/or Si-O-Mg deformation and bending

modes [34,35]. The bands at 3394 cm^{-1} and 1639 cm^{-1} are assigned to the stretching and bending of the OH groups of water molecules adsorbed to the bentonite surface. The broad band around 3630 cm^{-1} is attributed to the stretching vibration of the OH group coordinated with the Al^{3+} cations in the octahedral layer [33,36].

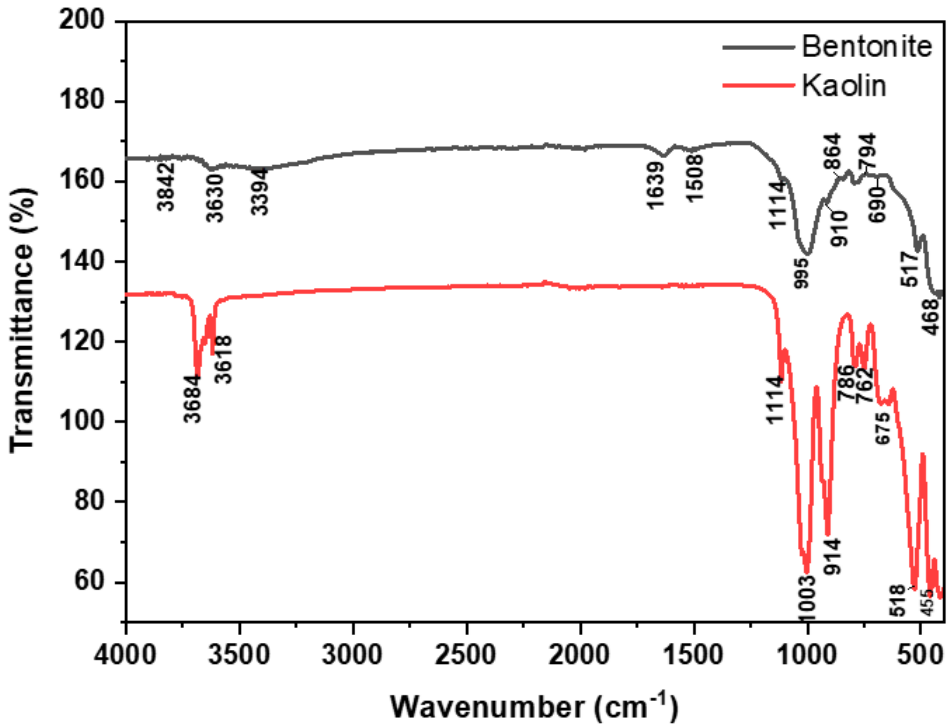

Figure 3. FTIR spectra of bentonite and kaolin.

The FTIR spectrum of kaolin shows bands at 1003 cm^{-1} and 548 $cm^{-1,}$ which can be assigned to Si-O-Al bonds, and that at 914 cm^{-1} corresponds to Al-OH. These bands are typical of the kaolinite mineral [26]. A sharp band at 1003 cm^{-1} is attributed to the Si-O stretching vibration, providing strong evidence of the presence of a silicate structure [33]. The bands at 3684 cm^{-1} and 3618 cm^{-1} correspond to the OH group stretching frequencies, while 1114 cm^{-1} and 455 cm^{-1} correspond to Si-O stretching [26]. The vibration at 455 cm^{-1} can be associated with the deformation mode of Si-O or Al-O bonds [31]. Both clays exhibit similar characteristic bands in the fingerprint region (794 cm^{-1} and 786 cm^{-1}) primarily due to the presence of impurities, like quartz, present in both clays [33,37]. The observed high Mg content in bentonite is supported by the EDS results, which also show a higher Mg content than Fe. The presence of quartz in both clays is further confirmed by SEM and HRTEM images in Figure 1, as well as the PXRD pattern in Figure 2.

3.4. XRF Characterization

The chemical composition of the clays, in weight percent (wt%), was determined using XRF, and the results are shown in Table 1. The trueness of the results was confirmed by the analysis of the certified reference material IPT-42 (São Simão, Brazil). The percentage relative standard deviation of the mineral components with a chemical composition of over 50% was 2%, while the rest of the compositions had a deviation of <7%. The presence of oxides such as CaO, MgO, MnO, and BaO indicates that neither material is a pure montmorillonite/kaolinite-containing clay. The clays contain traces of other minerals, such as quartz. The chemical composition of the selected samples reveals that they consist mainly of Al_2O_3, with 13.67% in bentonite and 37.75% in kaolin, and SiO_2, with 48.99% in kaolin and 58.19% in bentonite. These findings are in agreement with those reported by Kumar and Lingfa [37], where 2:1 clays (such as mica and smectite) showed a higher silica content and lower alumina than the 1:1 kaolinite group. However, both clays showed

relatively high silica content, which can be attributed to the presence of quartz [38]. The low presence of Na_2O, MgO, CaO, and K_2O in kaolin suggests that high-swelling clay minerals like montmorillonite are unlikely to be present [39]. The SiO_2/Al_2O_3 ratios for kaolin and bentonite were 1.29 and 4.3, respectively. A ratio below 2 is generally associated with the presence of the kaolinite mineral (1:1 clay), while ratios exceeding 2 typically indicate the presence of 2:1 clay minerals [40–42], which in this study is montmorillonite.

Table 1. Chemical composition of the clay weight (wt%).

Clay Type	Layer Type	Chemical Composition (wt%)											
		SiO_2	Al_2O_3	Fe_2O_3	TiO_2	CaO	MgO	K_2O	Na_2O	BaO	MnO	P_2O_5	L.O.I
Bentonite	2:1	58.19	13.67	2.43	0.16	0.97	2.32	1.03	2.34	0.16	0.07	0.06	18.32
Kaolin	1:1	48.99	37.75	0.44	1.41	0.15	-	0.10	-	-	-	0.07	14.27

Notably, a significant amount of Fe_2O_3 was observed in the bentonite clay, highlighting the presence of hematite [43]. These results align with the mineralogical data in Figure 2 and effectively validate the existence of various crystallized mineral phases, including quartz, montmorillonite, and kaolinite.

The CaO content in bentonite is comparatively lower than the levels of K_2O and Na_2O, suggesting that this particular type of clay can be classified as Na-bentonite [36]. The EDS data belowalso show that the Na amount (2.0%) is about four times higher than that of Ca (0.4%), further supporting this classification. Bentonite also contains oxides of Mg, Na, Ba, and Mn, which are not found in kaolin. Figure 4 displays the major chemical composition of the clays. It is evident that bentonite has a higher SiO_2 content compared to kaolin, while kaolin exhibits a higher Al_2O_3 content than bentonite. The LOI of bentonite is also greater than that of kaolin, indicating a higher water and organic matter content in bentonite compared to kaolin [13].

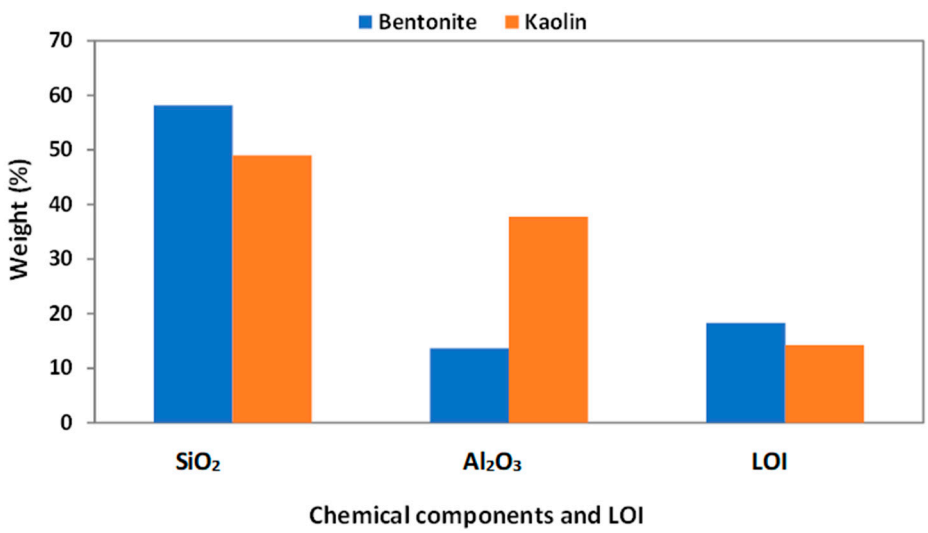

Figure 4. Major chemical components present in the clays and LOI.

3.5. EDS Analysis

The EDS was used to further confirm the chemical composition of the clays, and the results are shown in Figure 5.

The EDS results for bentonite confirm that Si and O are the major elements present in the clay, which aligns with the high SiO_2 chemical composition observed in the XRF results.

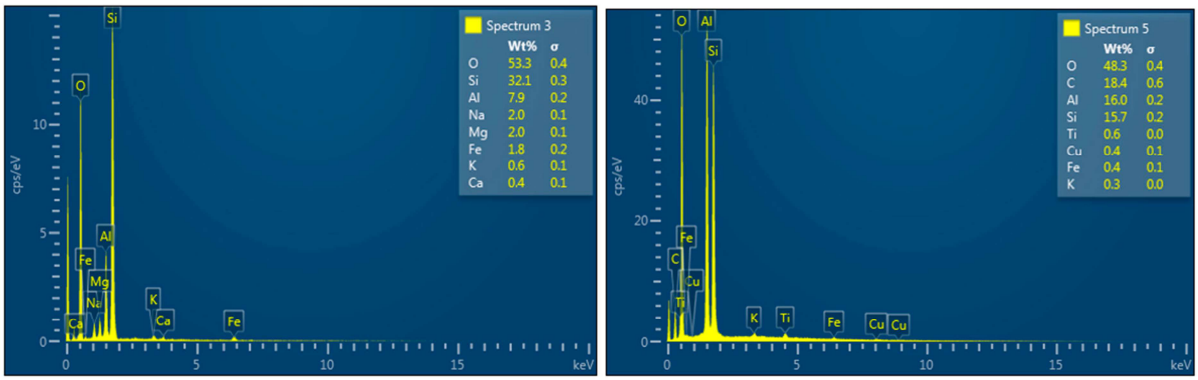

(**a**) (**b**)

Figure 5. The EDS spectra of (**a**) bentonite and (**b**) kaolin.

In kaolin, the EDS results indicate a higher Al content compared to Si, consistent with the XRF results where Al_2O_3 was identified as the major constituent of the clay. The EDS analysis also reveals that Na has the highest wt% among the exchangeable cations present in bentonite, confirming that the bentonite in this study can be classified as Na-bentonite. The (Na + K)/Ca is 6.5, further highlighting that the high-silica bentonite is enriched with potassium and sodium. This also further confirms the findings on the XRF data, where Na_2O showed a higher content than MgO, K_2O, and CaO. Sodium bentonite has a high swelling capacity and has proven to be efficient in several industrial applications [10]. On the other hand, kaolin only has K as the interchangeable cation, explaining its low CEC of just 13 cmol (+)/kg. In contrast, bentonite contains potassium, sodium, magnesium, and calcium in its structure, contributing to its high CEC of 78 cmol (+)/kg, as indicated by their respective data sheets.

3.6. BET Characterization

Figure 6 shows the adsorption/desorption curves of bentonite and kaolin observed under liquid nitrogen. Both clays depicted type IV N_2 adsorption–desorption isotherms, accompanied by a hysteresis loop, in accordance with the International Union of Pure and Applied Chemistry (IUPAC) classification [44].

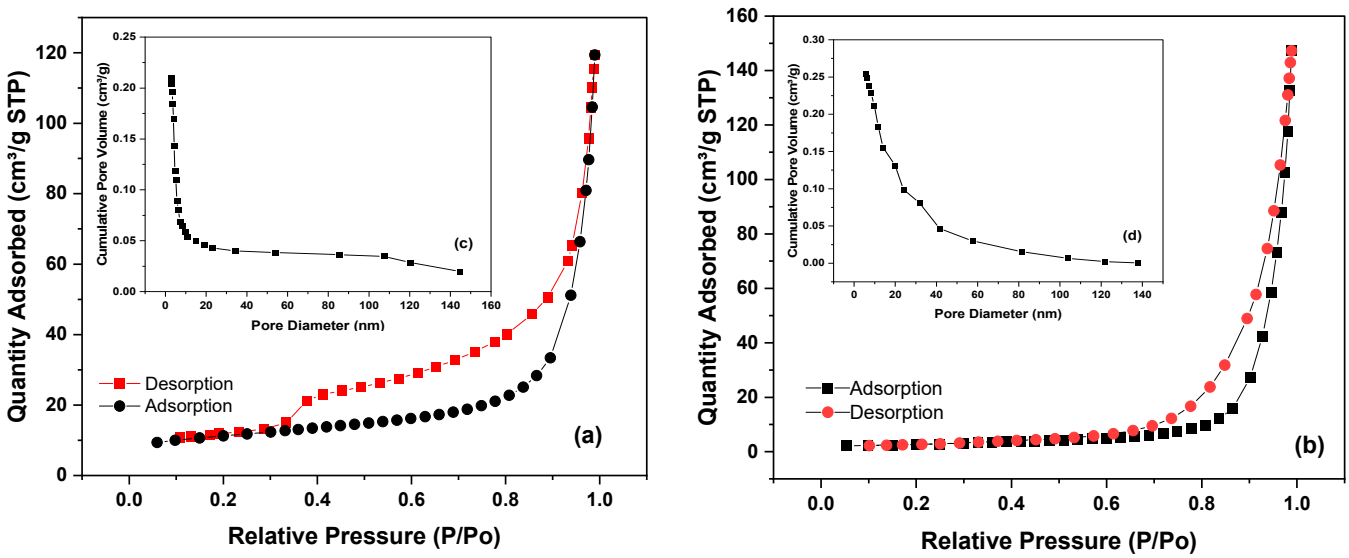

Figure 6. BET adsorption/desorption curves of (**a**) bentonite and (**b**) kaolin together with their BJH cumulative pore size distribution plots (**c**) bentonite and (**d**) kaolin.

The observed isotherms are characteristic of both mesoporous and macroporous materials [45], which is consistent with the SEM results presented in Figure 1. The relative pressure (P/P0) values of 0.35 for bentonite and 0.65 for kaolin correspond to the base of the hysteresis loop and signify the start of capillary condensation in the thinnest pores. As the P/P0 approaches 1, a sharp increase in the sorption curves can be observed, indicating the presence of larger pores in the material. The specific surface area, S_{BET}, was determined from isotherms using the BET equation [46]. The specific surface area of bentonite was found to be 38.7 m^2/g, while that of kaolin was 9.51 m^2/g. The high specific surface area of bentonite suggests its potential for applications such as the adsorption of toxic metal ions in water, as it provides sufficient active sites [47]. The BJH plot indicates the existence of a wide range of pore size distribution; both clays contain mesoporous (pores 2–50 nm in diameter) and macroporous (>50 nm) structures [48,49]. The size of the pores in the clay was not uniform. The kaolin pore sizes ranged between 5.68 and 138 nm, while the pore sizes for bentonite were in the range of 2.78–145 nm. The total pore volume and average pore size of bentonite were determined to be 0.185 cm^3/g and 29.6 nm, respectively, while the corresponding values for kaolin were 0.228 cm^3/g and 42.7 nm, respectively.

3.7. TGA Characterization

The thermal stability of the clays was determined using TGA with the thermal treatment of the clays carried out in the region of 25–1000 °C for 90 min. Figure 7 shows the thermograms.

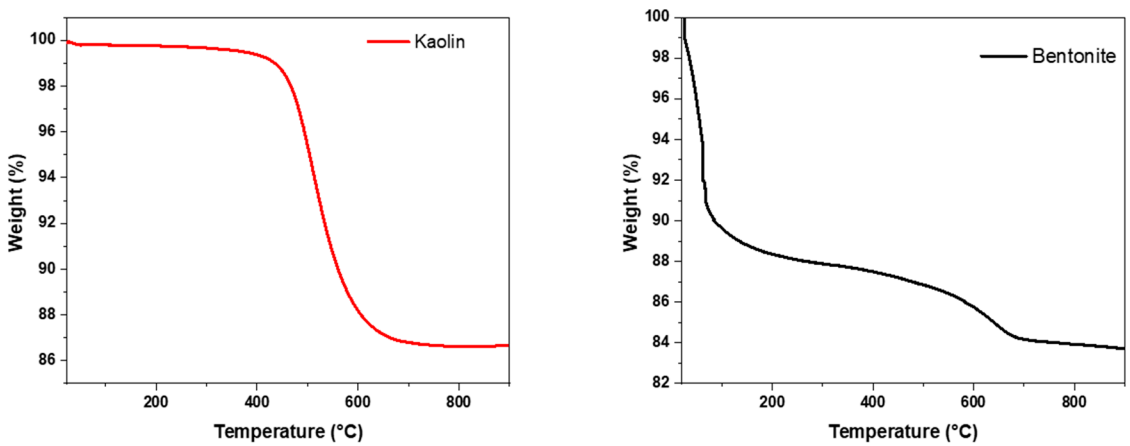

(**a**) (**b**)

Figure 7. TGA curves of (**a**) kaolin and (**b**) bentonite.

The TGA thermogram of kaolin shows two weight loss stages. The first stage, occurring at temperatures below 70 °C, corresponds to a pre-dehydroxylation weight loss (<1%), while the major weight loss (13.37%) occurs at around 500 °C and can be attributed to the dehydroxylation process [50]. These findings are similar to those reported by Wahyuni, Zissis, and Mouloungui [17], who reported a mass loss of 0.67% and 11.52% at 70 °C and 490 °C, respectively, on kaolin from West Kalimantan, Inperformedsia. Another study also reported dehydroxylation of kaolin between the temperatures of 430 and 650 °C, resulting in a mass loss of 9.3% and pre-dehydroxylation at 20–50 °C [50]. The TGA curve for bentonite reveals a two-stage weight loss. The initial weight loss (12.23%) occurring from 25 °C to 300 °C is attributed to the loss of surface water molecules and those intercalated in the clay's layer structure. The weight loss (4.85) at 350 °C to 800 °C is due to dehydroxylation and the decomposition of organic matter in the clay [35]. Similar results were reported by Al-Essa [33] in a study on bentonite clay from Al Azraq, Iraq, where a minor weight loss was observed at 30–200 °C due to absorbed and free water molecules, and a significant weight loss occurred between temperatures ranging from 325 °C to 720 °C, attributed to

dehydroxylation. Both clays exhibit similar weight loss percentages. However, based on their thermal stability, it can be deduced that bentonite has a higher water content than kaolin, which supports the XRF results in Table 1 and Figure 4.

3.8. Zeta Potential

The zeta potentials of the clay samples as a function of pH are given in Figure 8. The electrical charge of bentonite originates from pH-dependent adsorption/desorption reactions on the surface's hydroxyl groups and isomorphous substitutions within the clay structure [26].

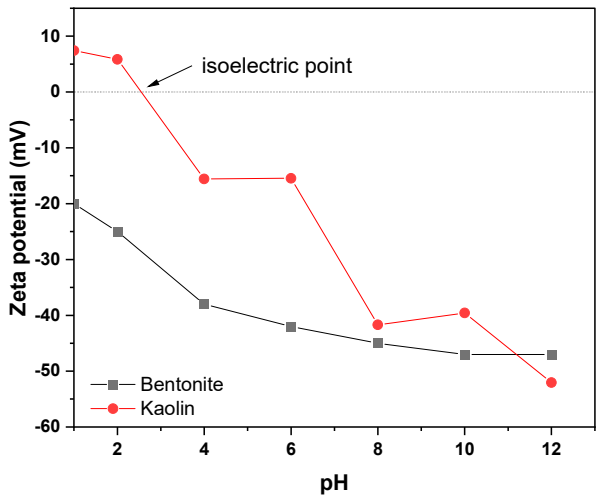

Figure 8. Zeta potential of kaolin and bentonite clays.

Although the negative charges on the structure of bentonite do not directly come into contact with the water solution, they do create a net negative electrical potential. This negative charge is primarily responsible for the clay particles possessing electrical, sorptive, and coagulative properties. Consequently, the zeta potential of bentonite remains negative across a wide range of pH levels, which is characteristic of particles with a structural negative charge [26,51]. As a result, the isoelectric point (IEP) value of bentonite could not be determined because it exhibits a negative electrical charge at all pH values. The zeta potential of the particles becomes more negative with increasing suspension pH.

On the other hand, the IEP value of kaolin is 2.4. The clay suspensions, in general, display relatively high stability due to the high negative surface charge of the particles. The significant zeta potential of the clays indicates their potential in the remediation of charged pollutants from the environment.

3.9. Particle Size Distribution

The particle size distribution was measured using two different techniques: HR-TEM imaging and DLS measurements. The results of these techniques are depicted in Figures 9 and 10. Figure 9 displays the HR-TEM particle size distribution curves for the two clay materials. Both samples exhibit a wide range of particle sizes. The particle size distribution histogram was constructed based on the analysis of 250 particles of bentonite and 135 particles of kaolin. The bentonite sample (Figure 9a) had a mean particle size of 73.6 nm with a standard deviation of 134.8 nm. Conversely, kaolin (Figure 9b) had a mean particle size of 214.5 nm with a standard deviation of 135.2 nm.

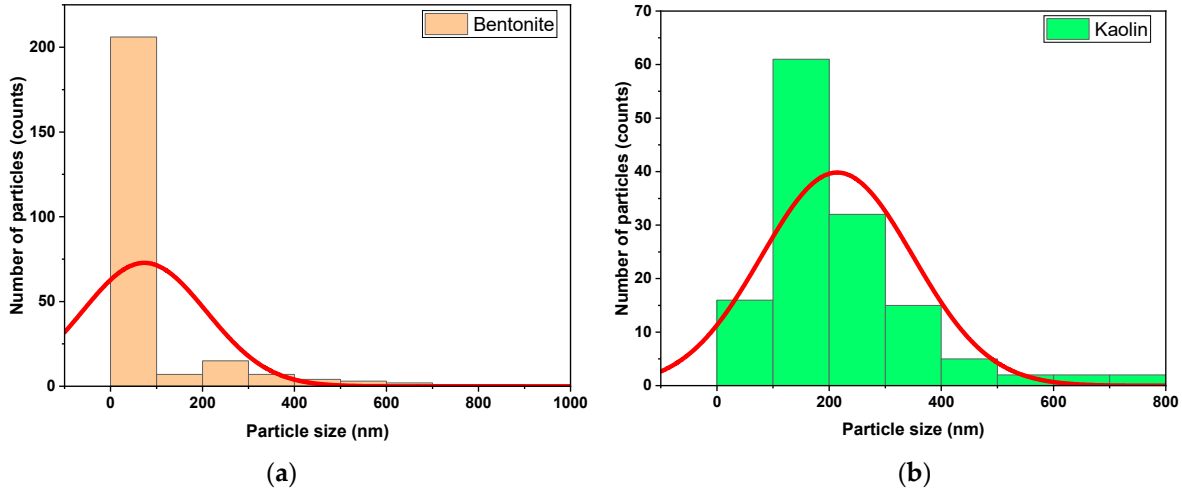

Figure 9. HR-TEM particle size distribution for (**a**) bentonite and (**b**) kaolin.

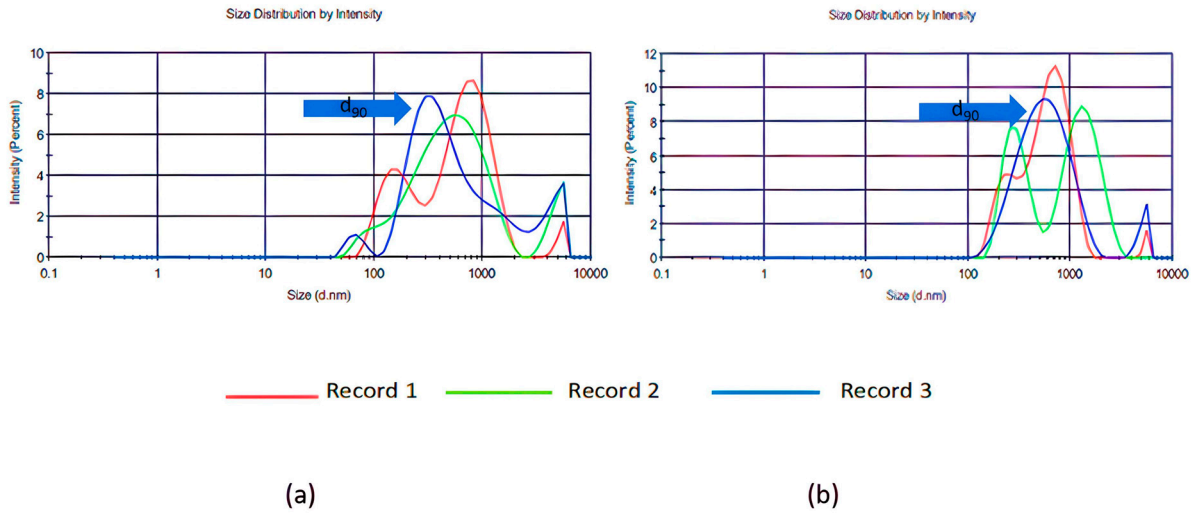

Figure 10. DLS particle size distribution for (**a**) bentonite and (**b**) kaolin.

The particle size distribution obtained using the DLS measurement is shown in Figure 10. The bentonite clay sample (Figure 10a) showed a broad, dispersed particle size distribution, while kaolin clay (Figure 10b) showed a bimodal distribution.

Figure 10 shows the DLS particle size distribution for (a) bentonite and (b) kaolin. The polydispersity index (PDI) for bentonite was 0.586, indicating a broad dispersity, whereas, for kaolin, it was 0.359, indicating moderate dispersity. The PDI values below 0.7 validate the reliability of the measurements [46]. The heterogeneity of the particles determined by the DLS is consistent with the results obtained from SEM and HRTEM presented in Figure 1, as well as the BET results depicted in Figure 6. Scanning electron microscopy and HRTEM images revealed particles of varying sizes and irregular shapes, while BET analysis identified the presence of mesoporous and macroporous structures. The DLS particle size distribution for bentonite clay showed that particles with a diameter of 606.9 nm constituted 82.7% of the total particles, while for kaolin clay, particles with a diameter of 610.3 nm accounted for 94.3% of the total particles present. Additionally, there were other particles of varying sizes present, measuring 5113 nm (5.7%) for kaolin and 4349 nm (13.5%), and 67.82 nm (3.8%) for bentonite.

For bentonite particle size distribution by DLS, the standard deviations for peak 1 (606.9 nm) and peak 2 (4349 nm) were 527.9 and 969.8, respectively. The lowest and acceptable standard deviation of 12.34 was obtained for peak 3 (67.82 nm). The DLS mean for kaolin is 575.l nm, while that of bentonite is 418.4 nm. These average sizes differ

significantly from those obtained through HRTEM measurements. Furthermore, there were additional particles of different sizes present in the clays. For kaolin, these included particles measuring 5113 nm (5.7% of the total) alongside the predominant 610.3 nm particles, while for bentonite, particles measuring 4349 nm (13.5%) and 67.82 nm (3.8%) were observed.

In terms of the particle size distribution determined by DLS for bentonite, the standard deviations for peak 1 (606.9 nm) and peak 2 (4349 nm) were 527.9 nm and 969.8 nm, respectively. Peak 3 (67.87 nm) showed the lowest and acceptable standard deviation of 12.34 nm. It has been reported in other studies that the DLS analysis, specifically the intensity parameter, tends to yield larger mean sizes and errors compared to the TEM measurements [52]. The average particle size obtained through DLS for kaolin was 575.1 nm (standard deviation of 312.9 nm), whereas for bentonite, it was 418.4 nm (standard deviation of 402.5 nm). These average particle sizes differ significantly from those obtained using HRTEM measurements.

The HRTEM mean particle size for kaolin was determined to be 214.5 nm (standard deviation of 350.2 nm), while for bentonite, it was 73.6 nm (standard deviation of 133.8 nm). Comparing these values to the DLS measurements, the DLS mean size for bentonite was over 400% higher than the HRTEM mean, whereas, for kaolin, the DLS mean size was approximately 160% higher than the HRTEM mean. It is important to note that the standard errors for the other parameters were larger as well. The values obtained from DLS tend to be much higher than those from HRTEM, as the DLS-intensity parameter shows values about five times larger than HRTEM [52,53]. Also, the presence of a dispersant in the sample leads to the enlargement of particle sizes, thereby inducing errors in DLS particle sizing measurements when compared to TEM analyses. This difference becomes more significant with an increase in the polydispersity of the sample, which explains why the DLS mean size for bentonite is considerably larger than the HRTEM mean when comparing the results to that of kaolin. Although both techniques present different challenges, the overall results indicate that bentonite has smaller particles compared to kaolin, and it also contains a large number of differently shaped and sized particles, as confirmed by both the HRTEM images and the PDI indexes obtained. Another technique, such as atomic force microscopy (AFM), is recommended to complement the two techniques described above [2,46,54].

4. Conclusions

This study aimed to characterize two South African clays for their chemical, mineralogical, and morphological structure. The results revealed that bentonite clay primarily consists of montmorillonite as the main mineral, along with impurities of quartz, anorthite/feldspar, and trace salts. On the other hand, kaolin clay mainly comprises kaolinite as the dominant mineral.

The chemical composition shows that bentonite has a high Na^+ content as the main interchangeable cation, while kaolin has minimal K^+ cations as the only interchangeable cation. The BET-N_2 adsorption isotherms indicate that both clays have mesoporous and macroporous structures, with bentonite having a higher specific surface area and pore volume. Bentonite's high surface area and negative charge, shown through BET analysis and zeta potential, make it a promising cost-effective and environmentally friendly potential toxic elements (PTES) adsorbent. Its porous structure can attract and trap positively charged PTEs. While kaolin's properties might be less appealing, modifications like activation and thermal treatment could improve its adsorption potential. Both clays exhibit thermal stability, indicating suitability for elevated temperature treatment processes. Future studies are recommended to explore their use in PTE removal. The results of these complementary techniques provide comprehensive and useful information on the properties and characteristics of bentonite and kaolin clays.

Author Contributions: Conceptualization, D.P.K. and A.A.A.; methodology, D.P.K. and A.A.A.; validation, D.P.K. and A.A.A.; formal analysis, D.P.K.; investigation, D.P.K. and A.A.A.; resources,

D.P.K. and A.A.A.; data curation, D.P.K.; writing—original draft preparation, D.P.K.; writing—review and editing, D.P.K. and A.A.A.; visualization, D.P.K. and A.A.A.; supervision, A.A.A.; project administration, A.A.A.; funding acquisition, A.A.A. All authors have read and agreed to the published version of the manuscript.

Funding: The research was funded by the Water Research Commission (WRC) of South Africa (project number C2022/2023-00933).

Institutional Review Board Statement: Not applicable.

Informed Consent Statement: Not applicable.

Data Availability Statement: All the data generated in this study have been reported in the manuscript.

Acknowledgments: Dipuo P. Kgabi expresses heartfelt gratitude towards the National Research Foundation (NRF) for its financial support. The University of Johannesburg's Central Analytical Facility (Spectrum) of the Faculty of Science and Research Centre for Synthesis and Catalysis are also acknowledged for their facilities.

Conflicts of Interest: The authors declare no conflict of interest.

References

1. Ochieng, O. Characterization and Classification of Clay Minerals for Potential Applications in Rugi Ward, Kenya. *Afr. J. Environ. Sci. Technol.* **2016**, *10*, 415–431. [CrossRef]
2. Sarkar, B.; Rusmin, R.; Ugochukwu, U.C.; Mukhopadhyay, R.; Manjaiah, K.M. *Modified Clay Minerals for Environmental Applications*; Elsevier Inc.: Amsterdam, The Netherlands, 2018; ISBN 9780128146187.
3. Biswas, B.; Juhasz, A.L.; Mahmudur Rahman, M.; Naidu, R. Modified Clays Alter Diversity and Respiration Profile of Microorganisms in Long-Term Hydrocarbon and Metal Co-Contaminated Soil. *Microb. Biotechnol.* **2020**, *13*, 522–534. [CrossRef] [PubMed]
4. Gu, S.; Kang, X.; Wang, L.; Lichtfouse, E.; Wang, C. Clay Mineral Adsorbents for Heavy Metal Removal from Wastewater: A Review. *Environ. Chem. Lett.* **2019**, *17*, 629–654. [CrossRef]
5. Kadİr, S.; Külah, T.; Erkoyun, H.; Christidis, G.E.; Arslanyan, R. Geology, Mineralogy, Geochemistry, and Genesis of Bentonite Deposits in Miocene Volcano–Sedimentary Units of the Balikesir Region, Western Anatolia, Turkey. *Clays Clay Miner.* **2019**, *67*, 371–398. [CrossRef]
6. Biswas, B.; Sarkar, B.; Rusmin, R.; Naidu, R. Bioremediation of PAHs and VOCs: Advances in Clay Mineral-Microbial Interaction. *Environ. Int.* **2015**, *85*, 168–181. [CrossRef]
7. Ahmad, S.; Yasin, K. Removal of Organic Pollutants by Using Surfactant Modified Bentonite. *J. Chem. Soc. Pak.* **2018**, *40*, 447–456.
8. Sun, L.; Ling, C.Y.; Lavikainen, L.P.; Hirvi, J.T.; Kasa, S.; Pakkanen, T.A. Influence of Layer Charge and Charge Location on the Swelling Pressure of Dioctahedral Smectites. *Chem. Phys.* **2016**, *473*, 40–45. [CrossRef]
9. Idoko, O.; Ajana, M.O.; Gushit, J.S.; Jock, A. Adsorption of Heavy Metals (Lead Ion) from Industrial Waste Water Using Acidified Bentonite Clay. *Int. J. Eng. Appl. Sci. Technol.* **2019**, *04*, 394–401. [CrossRef]
10. Muhammad, N.; Siddiqua, S. Calcium Bentonite vs. Sodium Bentonite: The Potential of Calcium Bentonite for Soil Foundation. *Mater. Today Proc.* **2022**, *48*, 822–827. [CrossRef]
11. Barbooti, M.M. Simultaneous Removal of Chromium and Lead from Water by Sorption on Iraqi Montmorillonite. *J. Environ. Prot.* **2015**, *6*, 237–249. [CrossRef]
12. Hernández, A.C.; Sánchez-Espejo, R.; Meléndez, W.; González, G.; López-Galindo, A.; Viseras, C. Characterization of Venezuelan Kaolins as Health Care Ingredients. *Appl. Clay Sci.* **2019**, *175*, 30–39. [CrossRef]
13. Akisanmi, P.; Akisanmi, P. Classification of Clay Minerals. *Mineralogy* **2022**, 3–9. [CrossRef]
14. Birnin Yauri, U.A.; Faruq, U.Z.; Noma, S.S.; Sharif, V. Characterization of Dabagi Clay Deposit for Its Ceramics Potential. *Afr. J. Environ. Sci. Technol.* **2014**, *8*, 455–459. [CrossRef]
15. da Silva Favero, J.; dos Santos, V.; Weiss-Angeli, V.; Gomes, L.B.; Veras, D.G.; Dani, N.; Mexias, A.S.; Bergmann, C.P. Evaluation and Characterization of Melo Bentonite Clay for Cosmetic Applications. *Appl. Clay Sci.* **2019**, *175*, 40–46. [CrossRef]
16. Tadesse, S.H. Application of Ethiopian Bentonite for Water Treatment Containing Zinc. *Emerg. Contam.* **2022**, *8*, 113–122. [CrossRef]
17. Wahyuni, N.; Zissis, G.; Mouloungui, Z. Characterization of Acid Sites on Modified Kaolinite by FTIR Spectra of Pyridine Adsorbed. *AIP Conf. Proc.* **2018**, *2026*, 020042. [CrossRef]
18. Liu, X.; Hicher, P.; Muresan, B.; Saiyouri, N.; Hicher, P.Y. Heavy Metal Retention Properties of Kaolin and Bentonite in a Wide Range of Concentration and Different PH Conditions. *Appl. Clay Sci.* **2016**, *119*, 365–374. [CrossRef]
19. Mulaba-Bafubiandi, A.F.; Hlekane, P.X.D.A. Characterisation of Traditional Ceramic Materials Used in the Sotho Culture (South Africa) for Clay Pot Making. In Proceedings of the SAIP 2015, Port Elizabeth, South Africa, 29 June–3 July 2015; pp. 79–83.
20. Diko-Makia, L.; Ligege, R. Composition and Technological Properties of Clays for Structural Ceramics in Limpopo (South Africa). *Minerals* **2020**, *10*, 700. [CrossRef]

21. Coetzee, P.P.; Coetzee, L.L.; Puka, R.; Mubenga, S. Characterisation of Selected South African Clays for Defluoridation of Natural Waters. *Water SA* **2003**, *29*, 331–338. [CrossRef]
22. Morekhure-Mphahlele, R.; Focke, W.W.; Grote, W. Characterisation of Vumba and Ubumba Clays Used for Cosmetic Purposes. *S. Afr. J. Sci.* **2017**, *113*, 2–6. [CrossRef]
23. Abukhadra, M.R.; Refay, N.M.; El-Sherbeeny, A.M.; Mostafa, A.M.; Elmeligy, M.A. Facile Synthesis of Bentonite/Biopolymer Composites as Low-Cost Carriers for 5-Fluorouracil Drug; Equilibrium Studies and Pharmacokinetic Behavior. *Int. J. Biol. Macromol.* **2019**, *141*, 721–731. [CrossRef] [PubMed]
24. García-Romero, E.; Suárez, M. A Structure-Based Argument for Non-Classical Crystal Growth in Natural Clay Minerals. *Miner. Mag.* **2018**, *82*, 171–180. [CrossRef]
25. Pan, X.; Li, S.; Li, Y.; Guo, P.; Zhao, X.; Cai, Y. Resource, Characteristic, Purification and Application of Quartz: A Review. *Miner. Eng.* **2022**, *183*, 107600. [CrossRef]
26. Gan, C.; Hu, H.; Meng, Z.; Zhu, X.; Gu, R.; Wu, Z.; Wang, H.; Wang, D.; Gan, H.; Wang, J.; et al. Characterization and Hemostatic Potential of Two Kaolins from Southern China. *Molecules* **2019**, *24*, 3160. [CrossRef] [PubMed]
27. Maged, A.; Kharbish, S.; Ismael, I.S.; Bhatnagar, A. Characterization of Activated Bentonite Clay Mineral and the Mechanisms Underlying Its Sorption for Ciprofloxacin from Aqueous Solution. *Environ. Sci. Pollut. Res.* **2020**, *27*, 32980–32997. [CrossRef]
28. Huggett, J.M. Clay Minerals. *Ref. Modul. Earth Syst. Environ. Sci.* **2015**, *40*, 358–365. [CrossRef]
29. Zhirong, L.; Azhar Uddin, M.; Zhanxue, S. FT-IR and XRD Analysis of Natural Na-Bentonite and Cu(II)-Loaded Na-Bentonite. *Spectrochim. Acta A Mol. Biomol. Spectrosc.* **2011**, *79*, 1013–1016. [CrossRef]
30. Chandra, U.; Pandey, K.K.; Parthasarathy, G.; Sharma, S.M. High-Pressure Investigations on Piplia Kalan Eucrite Meteorite Using in-Situ X-Ray Diffraction and 57Fe Mössbauer Spectroscopic Technique up to 16 GPa. *Geosci. Front.* **2016**, *7*, 265–271. [CrossRef]
31. Caponi, N.; Carvalho Collazzo, G.; Luiz Jahn, S.; Dotto, G.L.; Mazutti, M.A.; Foletto, E.L. Use of Brazilian Kaolin as a Potential Low-Cost Adsorbent for the Removal of Malachite Green from Colored Effluents. *Mater. Res.* **2017**, *20*, 14–22. [CrossRef]
32. Ravindra Reddy, T.; Kaneko, S.; Endo, T.; Lakshmi Reddy, S. Spectroscopic Characterization of Bentonite. *J. Lasers Opt. Photonics* **2017**, *4*, 171. [CrossRef]
33. Al-Essa, K. Activation of Jordanian Bentonite by Hydrochloric Acid and Its Potential for Olive Mill Wastewater Enhanced Treatment. *J. Chem.* **2018**, *2018*, 8385692. [CrossRef]
34. Al-Essa, K.; Al-Essa, E.M. Effective Approach of Activated Jordanian Bentonite by Sodium Ions for Total Phenolic Compounds Removal from Olive Mill Wastewater. *J. Chem.* **2021**, *2021*, 7405238. [CrossRef]
35. Hebbar, R.S.; Isloor, A.M.; Prabhu, B.; Inamuddin; Asiri, A.M.; Ismail, A.F. Removal of Metal Ions and Humic Acids through Polyetherimide Membrane with Grafted Bentonite Clay. *Sci. Rep.* **2018**, *8*, 4665. [CrossRef]
36. El-Mahalaway, A.M.; El-Azab, N.E.; Abdrabbo, M.; Said, O.M.; Sabry, D. Sorption Characteristics of Iron, Fluoride and Phosphate from Wastewater of Phosphate Fertilizer Plant Using Natural Sodium Bentonite. *J. Membr. Sci. Technol.* **2018**, *8*, 3. [CrossRef]
37. Kumar, A.; Lingfa, P. Sodium Bentonite and Kaolin Clays: Comparative Study on Their FT-IR, XRF, and XRD. *Mater. Today Proc.* **2020**, *22*, 737–742. [CrossRef]
38. Hedfi, I.; Hamdi, N.; Srasra, E.; Rodriguez, M.A. The Preparation of Micro-Porous Membrane from a Tunisian Kaolin. *Appl. Clay Sci.* **2014**, *101*, 574–578. [CrossRef]
39. Oumar, K.O.; Gilbert François, N.N.; Bertrand, M.M.; Nathanael, T.; Constantin, B.E.; Simon, M.J.; Jacques, E. Mineralogical, Geochemical Characterization and Physicochemical Properties of Kaolinitic Clays of the Eastern Part of the Douala Sub-Basin, Cameroon, Central Africa. *Appl. Sci.* **2022**, *12*, 9143. [CrossRef]
40. Pierre, T.J.; Pierre, N.J.; Achile, B.M.; Djakba, B.S.; Lucien, B.D. Morphological, Physico Chemical, Mineralogical and Geochemical Properties of Vertisols Used in Bricks Production in the Logone Valley (Cameroon, Central Africa). *Int. Res. J. Geol. Min.* **2015**, *5*, 20–30. [CrossRef]
41. Tsozué, D.; Nzeugang, A.N.; Mache, J.R.; Loweh, S.; Fagel, N. Mineralogical, Physico-Chemical and Technological Characterization of Clays from Maroua (Far-North, Cameroon) for Use in Ceramic Bricks Production. *J. Build. Eng.* **2017**, *11*, 17–24. [CrossRef]
42. Ravisankar, R.; Naseerutheen, A.; Rajalakshmi, A.; Raja Annamalai, G.; Chandrasekaran, A. Application of Thermogravimetry–Differential Thermal Analysis (TG–DTA) Technique to Study the Ancient Potteries from Vellore Dist, Tamilnadu, India. *Spectrochim. Acta A Mol. Biomol. Spectrosc.* **2014**, *129*, 201–208. [CrossRef]
43. Hmeid, H.A.; Akodad, M.; Baghour, M.; Moumen, A.; Skalli, A.; Azizi, G. Experimental Design and Modeling of Removal of Organic Matter and Nutrients in the OMW by Calcium Bentonite. *E3S Web Conf.* **2021**, *234*, 00092. [CrossRef]
44. Abebe, B.; Murthy, H.C.A.; Amare, E. Summary on Adsorption and Photocatalysis for Pollutant Remediation: Mini Review. *J. Encapsulation Adsorpt. Sci.* **2018**, *8*, 225–255. [CrossRef]
45. Alothman, Z.A. A Review: Fundamental Aspects of Silicate Mesoporous Materials. *Materials* **2012**, *5*, 2874–2902. [CrossRef]
46. Dinh, V.P.; Nguyen, P.T.; Tran, M.C.; Luu, A.T.; Hung, N.Q.; Luu, T.T.; Kiet, H.A.T.; Mai, X.T.; Luong, T.B.; Nguyen, T.L.; et al. HTDMA-Modified Bentonite Clay for Effective Removal of Pb(II) from Aqueous Solution. *Chemosphere* **2022**, *286*, 131766. [CrossRef] [PubMed]
47. Hussain, S.T.; Khaleefa Ali, S.A. Removal of Heavy Metal by Ion Exchange Using Bentonite Clay. *J. Ecol. Eng.* **2020**, *22*, 104–111. [CrossRef]

48. Mirzaei, A.; Janghorban, K.; Hashemi, B.; Hosseini, S.R.; Bonyani, M.; Leonardi, S.G.; Bonavita, A.; Neri, G. Synthesis and Characterization of Mesoporous α-Fe_2O_3 Nanoparticles and Investigation of Electrical Properties of Fabricated Thick Films. *Process. Appl. Ceram.* **2016**, *10*, 209–218. [CrossRef]
49. Tang, J.; Wang, J. Fe-Based Metal Organic Framework/Graphene Oxide Composite as an Efficient Catalyst for Fenton-like Degradation of Methyl Orange. *RSC Adv.* **2017**, *7*, 50829–50837. [CrossRef]
50. Saukani, M.; Arief, S.; Syahrillah, G.R.F.; Hidayat, N. The Low Concentration of Sodium Hydroxide Influence on the Compressive Strength of Fly Ash/Natural Kaolin-Based Geopolymer. *IOP Conf. Ser. Mater. Sci. Eng.* **2019**, *515*, 012063. [CrossRef]
51. Au, P.I.; Leong, Y.K. Rheological and Zeta Potential Behaviour of Kaolin and Bentonite Composite Slurries. *Colloids Surf. A Physicochem. Eng. Asp.* **2013**, *436*, 530–541. [CrossRef]
52. Souza, T.G.F.; Ciminelli, V.S.T.; Mohallem, N.D.S. A Comparison of TEM and DLS Methods to Characterize Size Distribution of Ceramic Nanoparticles. *J. Phys. Conf. Ser.* **2016**, *733*, 012039. [CrossRef]
53. Wilson, B.K.; Prud'homme, R.K. Nanoparticle Size Distribution Quantification from Transmission Electron Microscopy (TEM) of Ruthenium Tetroxide Stained Polymeric Nanoparticles. *J. Colloid. Interface Sci.* **2021**, *604*, 208–220. [CrossRef] [PubMed]
54. Uddin, M.K. A Review on the Adsorption of Heavy Metals by Clay Minerals, with Special Focus on the Past Decade. *Chem. Eng. J.* **2017**, *308*, 438–462. [CrossRef]